Dalton Transactions

ROYAL SOCIETY OF CHEMISTRY

PAPER

View Article Online
View Journal | View Issue

Check for updates

Cite this: *Dalton Trans.*, 2025, **54**, 3610

Homochiral layered indium phosphonates: solvent modulation of morphology and chiral discrimination adsorption†

Qian Teng, Song-Song Bao, Ran Gao and Li-Min Zheng *

Received 18th November 2024,
Accepted 9th January 2025

DOI: 10.1039/d4dt03227f

rsc.li/dalton

Assembling chiral coordination polymers into nano/microflower structures may improve their performance in applications such as chiral recognition and separation. In this study, we chose a chiral metal phosphonate system, *i.e.*, $In(NO_3)_3$/*R*-, *S*-pempH$_2$ [pempH$_2$ = (1-phenylethylamino)methylphosphonic acid], and carried out systematic work on the self-assembly of this system in different alcohol/H_2O mixed solvents under solvothermal conditions. Enantiomeric compounds *R*-, *S*-$[In_2(pempH)_2(\mu_2\text{-}OH)_2(H_2O)_2](NO_3)_2$ (***R*-**, ***S*-1**) were obtained showing dense layered structures, but their morphologies varied with alcohol solvent. We obtained crystals of ***R*-**, ***S*-1C** in triethylene glycol (TEG)/H_2O mixed solvent and spiral microflowers of ***R*-**, ***S*-1MF** in isopropanol (IPA)/H_2O mixed solvent. Adsorption isotherms using enantiopure *R*-2-butanol and *S*-2-butanol as probe molecules revealed that compounds ***R*-1MF** and ***S*-1MF** had higher adsorption capacity compared to the crystalline sample and displayed enantioselective adsorption behaviour.

Published on 10 January 2025. Downloaded on 2/21/2026 7:01:00 PM.

Introduction

Chiral materials have attracted considerable attention owing to their potential applications in fields such as enantioselective separation, chiral sensing and asymmetric catalysis.[1–5] Chiral porous metal–organic frameworks (MOFs) or coordination polymers (CPs) are ideal candidates for chiral recognition and separation because their structures can be designed and modified to provide a pore environment for specific chiral guests.[6–8] However, achieving precise and uniformly distributed pore structure characteristics in three-dimensional (3D) chiral MOFs is not only challenging, but also highly selective towards the size and shape of chiral guest molecules, thus restricting their adaptability to diverse chiral molecular systems. A feasible solution is to prepare two-dimensional (2D) chiral MOFs or CPs and further exfoliate them into nanosheets.[9–11] The unique structural characteristics of nanosheets enable them to exhibit large surface areas, which greatly increases the adsorption sites of chiral MOF materials and allows them to be used for the recognition and separation of chiral molecules of different sizes. A notable example is given by Cui and co-workers, who fabricated nanosheets of Eu-MOF based on a chiral 1,1′-biphenyl phosphoric acid that can be used as chiral optical sensors for the detection of chiral terpenes and terpenoids.[12] Nevertheless, despite significant progress in this direction, challenges still remain in synthesizing 2D materials with permanent chirality, good solubility and stability. In particular, the re-stacking of chiral nanosheets reduces the pore size, decreases the surface area, deteriorates the solubility, and ultimately results in the formation of bulk 3D materials. We envision that assembling nanosheets into nano-/micro-structures can effectively avoid the re-stacking of chiral nanosheets. In addition, whether the chirality can be transferred and amplified from the nanosheets to the macroscopic assemblies is also an extremely intriguing question.

Previous studies have shown that chiral materials with flower-like structures can exhibit macroscopic chirality, high specific surface area, and certain spatially restricted domains. As a result, both the chiroptical and selective adsorption properties of the material may be improved.[13–15] For instance, chiral CuO@CNC nanoflowers exhibit prominent circularly polarized luminescence (CPL) properties and can effectively induce enantioselective crystallization of L-threonine.[16] We conceived that assembling chiral CP nanosheets into nano/microflowers might improve the chiral recognition performance of the materials, but similar studies have never been reported.

In this work, we carried out a systematic investigation on the $In(NO_3)_3$/*R*-, *S*-pempH$_2$ system, where *R*-, *S*-pempH$_2$ represent *R*-, *S*-(1-phenylethylamino)methylphosphonic acids. The In^{3+} ion and monophosphonate ligands were chosen because they can easily form dense layered structures and exhibit high thermal and water stability, akin to other metal phosphonates.[17–19] We performed the same reaction in

State Key Laboratory of Coordination Chemistry, School of Chemistry and Chemical Engineering, Nanjing University, Nanjing 210023, P. R. China.
E-mail: lmzheng@nju.edu.cn

†Electronic supplementary information (ESI) available. CCDC 2402002. For ESI and crystallographic data in CIF or other electronic format see DOI: https://doi.org/10.1039/d4dt03227f

This journal is © The Royal Society of Chemistry 2025

Published on 10 January 2025. Downloaded on 2/21/2026 7:01:00 PM.

different alcohol/H_2O solvents, where the alcohol can be methanol (MeOH), ethanol (EtOH), *n*-propanol (NPA), isopropanol (IPA), *n*-butanol (NBA), and triethylene glycol (TEG). In all cases, compounds *R*-, *S*-$[In_2(pempH)_2(\mu_2\text{-}OH)_2(H_2O)_2](NO_3)_2$ (***R***-, ***S*-1**) were obtained but with different morphologies. Specifically, we obtained crystals of ***R***-, ***S*-1** in TEG/H_2O mixed solvent (named ***R***-, ***S*-1C**, where C refers to crystal) and spiral microflowers in IPA/H_2O mixed solvent (named ***R***-, ***S*-1MF**, where MF refers to microflower) (Scheme 1). The acquisition of ***R***-, ***S*-1MF** spiral microflowers is impressive because it implies that the chirality has been successfully transferred and amplified from the chiral ligand to the chiral layer and eventually to the macroscopic morphology. We further investigated the formation mechanism of ***R***-, ***S*-1MF** and their chiral adsorption properties. It is noteworthy that although many chiral metal phosphonates are known in the literature,[20] chiral indium phosphonates have never been reported. Therefore, this work not only reports the first example of chiral indium phosphonates, but also the first example of chiral CPs with a nano/microflower morphology.

Experimental

Materials and methods

All starting materials were of analytical reagent grade and used as received without further purification. *R*-, *S*-(1-Phenylethylamino)methylphosphonic acids (*R*-, *S*-$pempH_2$) were prepared according to methods reported in the literature.[21,22] Elemental analyses of C, N and H were performed with an Elementar vario Macro cube. Fourier transform infrared (IR) spectra were recorded using KBr pellets on a Bruker Tensor 27 spectrometer in the range of 400–4000 cm^{-1}. Thermogravimetric analysis (TGA) was performed on a Mettler-Toledo TGA/DSC instrument in the range of 30–600 °C under a nitrogen flow at a heating rate of 5 °C min^{-1}. Powder X-ray diffraction (PXRD) data were recorded on a Bruker D8 ADVANCE X-ray powder diffractometer (Cu-Kα) at room temperature. The scanning electron microscope (SEM) images were recorded on a Hitachi S-4800. Transmission electron microscopy (TEM) measurements were performed on a JEM-2100. UV-vis spectra were recorded on a Shimadzu UV-3600 spectrometer. Electronic circular dichroism (ECD) spectra were recorded on a JASCO J-810 spectrophotometer at room temperature. The gas absorption and desorption isotherms were recorded on a BELSORP-Max adsorption analyzer in easy mode.

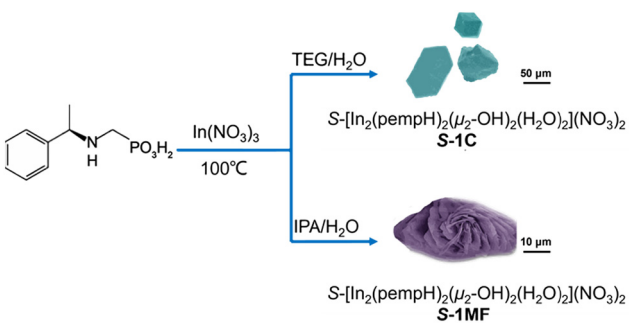

Scheme 1 Synthetic routes to ***S*-1C** and ***S*-1MF** in mixtures of TEG/H_2O and IPA/H_2O.

Single crystal X-ray crystallography

A suitable single crystal of ***S*-1C** was mounted on a loop ring, and diffraction data were collected using a Bruker D8 Venture diffractometer (Ga-Kα radiation, λ = 1.34138 Å). The collected data were integrated using the Siemens SAINT program,[23] and adsorption corrections were applied. The structures were solved using the intrinsic phasing method and refined on F^2 using full-matrix least-squares with the SHELXTL software package.[24] All the non-hydrogen atoms were refined anisotropically, while hydrogen atoms bound to carbon atoms and oxygen atoms of hydroxide were refined isotropically in the riding mode. CCDC for ***S*-1C** (no. 2402002†) contains the supplementary crystallographic data for this paper. Details of the crystal data and refinements of ***S*-1C** are summarized in Table S1,† and selected bond lengths and angles of ***S*-1C** in Table S2.†

Synthesis of *R*-, *S*-$[In_2(pempH)_2(\mu_2\text{-}OH)_2(H_2O)_2](NO_3)_2$ crystals (*R*-, *S*-1C)

Compounds ***R*-1C** and ***S*-1C** were synthesized in a similar way except for the different enantiomers of the ligands, so the synthesis of ***S*-1C** is described as a representative. *S*-$pempH_2$ (21.5 mg, 0.1 mmol) was added to 5 mL deionized water in a 20 mL glass vial. After heating at 100 °C for 3 hours, a clear solution was obtained because of the dissolution of the ligand. Then, 100 μL triethylene diamine solution (4 M) was added to adjust the pH to 3.2, followed by the addition of 5 mL TEG. After the solution was mixed uniformly, $In(NO_3)_3{\cdot}5H_2O$ (60 mg, 0.2 mmol) was added and the glass vial was sealed. The mixture was placed at 100 °C for 24 hours, and transparent block-like crystals of ***S*-1C** were obtained. Yield: 16 mg, 74.4% (based on *S*-$pempH_2$). Elemental analysis calcd (%) for $C_{18}H_{32}In_2N_4O_{16}P_2$ (***S*-1C**): C, 25.37; H, 3.79; N, 6.58%; found: C, 25.18; H, 3.88; N, 6.50%. IR (KBr, cm^{-1}): 3575(m), 3535(m), 3041(w), 2991(w), 2950(w), 2786(w), 2540(w), 2424(w), 2362(w), 1760(w), 1604(m), 1499(w), 1383(m), 1340(m), 1279(w), 1209(w), 1151(m), 1124(m), 1082(m), 1034(m), 995(m), 820(w), 788(w), 762(w), 702(w), 576(w), 492(w). For ***R*-1C**, yield: 14 mg, 65.1% (based on *R*-$pempH_2$). Elemental analysis calcd (%) for $C_{18}H_{32}In_2N_4O_{16}P_2$ (***R*-1C**): C, 25.37; H, 3.79; N, 6.58%; found: C, 25.09; H, 3.90; N, 6.49%. IR (KBr, cm^{-1}): 3572(m), 3537(m), 3039(w), 2988(w), 2942(w), 2785(w), 2537(w), 2424(w), 2364(w), 1760(w), 1605(m), 1500(w), 1386(m), 1342(m), 1277(w), 1207(w), 1154(m), 1124(m), 1081(m), 1033(m), 996(m), 823(w), 785(w), 763(w), 703(w), 572(w), 490(w).

Synthesis of *R*-,*S*-$[In_2(pempH)_2(\mu_2\text{-}OH)_2(H_2O)_2](NO_3)_2$ microflowers (*R*-, *S*-1MF)

Compounds ***R*-1MF** and ***S*-1MF** were synthesized in a similar way except for the different enantiomers of the ligands, so the synthesis of ***S*-1MF** is described as a representative. ***S*-1MF** was

Published on 10 January 2025. Downloaded on 2/21/2026 7:01:00 PM.

synthesized in the same manner as ***S*-1C**, except that the reaction solution was 90 vol% IPA/H_2O. Yield: 19 mg, 88.4% (based on *S*-pempH$_2$). Elemental analysis calcd (%) for $C_{18}H_{32}In_2N_4O_{16}P_2$ (***S*-1MF**): C, 25.37; H, 3.79; N, 6.58%; found: C, 25.37; H, 3.89; N, 6.39%. IR (KBr, cm^{-1}): 3572(m), 3536(m), 3037(w), 2990(w), 2950(w), 2788(w), 2533(w), 2424(w), 2362(w), 1760(w), 1608(m), 1497(w), 1385(m), 1337(m), 1277(w), 1207(w), 1156(m), 1124(m), 1081(m), 1032(m), 997(m), 826(w), 788(w), 756(w), 701(w), 574(w), 490(w). For ***R*-1MF**, yield: 17 mg, 79.1% (based on *R*-pempH$_2$). Elemental analysis calcd (%) for $C_{18}H_{32}In_2N_4O_{16}P_2$ (***R*-1MF**): C, 25.37; H, 3.79; N, 6.58%; found: C, 25.70; H, 3.90; N, 6.41%. IR (KBr, cm^{-1}): 3574(m), 3538(m), 3036(w), 2988(w), 2948(w), 2785(w), 2536(w), 2426(w), 2358(w), 1758(w), 1605(m), 1498(w), 1386(m), 1337(m), 1278(w), 1210(w), 1154(m), 1126(m), 1085(m), 1032(m), 995(m), 818(w), 788(w), 758(w), 705(w), 577(w), 493(w).

Results and discussion

Synthesis and characterization of *R*-1C and *S*-1C crystals

We initially synthesized block-like crystals of ***R*-**, ***S*-1C** through a solvothermal reaction of In(NO$_3$)$_3$·5H$_2$O and *R*- or *S*-pempH$_2$ (molar ratio 2 : 1) in 50 vol% TEG/H_2O at 100 °C. The phase purity of the bulk sample was confirmed by their powder X-ray diffraction (PXRD) patterns and elemental analyses (Fig. 1a). To examine the effect of the metal : ligand molar ratio and TEG/H_2O solvent ratio on the reaction product, we conducted similar experiments using the *S*-pempH$_2$ ligand. When the molar ratio was 1 : 1, we obtained the same material of ***S*-1C** as verified by the identical PXRD patterns (Fig. S1†), but the crystal quality was relatively poor. The reaction products obtained in 20–90 vol% TEG/H_2O mixed solvents were also the same (Fig. S2 and S3†).

Compounds ***R*-1C** and ***S*-1C** exhibit identical PXRD patterns and IR and UV-vis spectra (Fig. 1a, b and S4–S6†). The UV-Vis spectra show absorption peaks at 225 nm and 252 nm, attributed to the $\pi \rightarrow \pi^*$ transitions of the benzene rings in the ligands, characteristic of the B band.[25] The solid-state circular dichroism (CD) spectra of ***R*-1C** and ***S*-1C** show mirror dichroic signals at *ca.* 230 nm, demonstrating their enantiomeric nature (Fig. 1c). We further conducted thermogravimetric analysis and found that the two compounds were stable up to *ca.* 150 °C under an N_2 atmosphere (Fig. S7†). The weight losses of ***R*-1C** and ***S*-1C** between 170 and 210 °C were 6.5% and 6.4%, respectively, which are close to the calculated value of 6.3% after removal of three water molecules. From the single crystal structural analysis given below, we noted that there are only two coordination water molecules in the structure, so the third water molecule should come from the coordinated μ-OH, which may reduce the stability of the layered structure. Indeed, the compounds continued to lose weight above 210 °C, with acceleration above 230 °C, accompanied by decomposition of the organic components and collapse of the structure.

Since ***R*-1C** and ***S*-1C** are enantiomers, we only measured the single crystal structure of ***S*-1C**. It crystallizes in the mono-

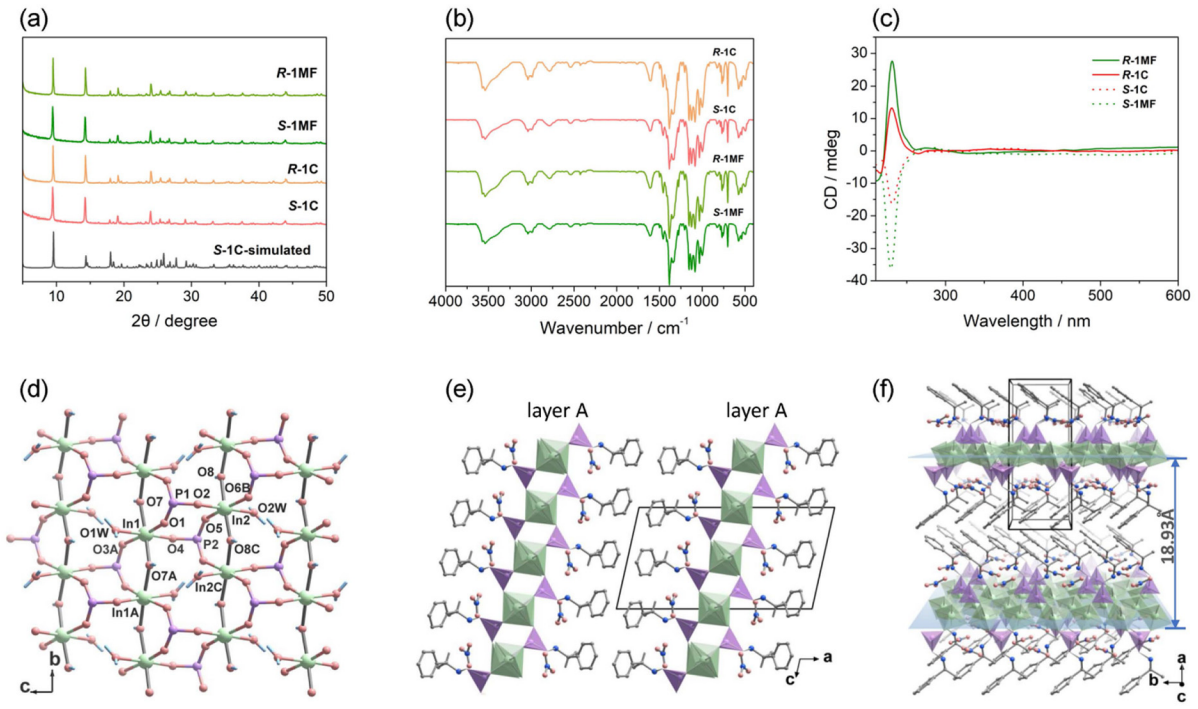

Fig. 1 (a) PXRD patterns of the as-synthesized compounds ***R*-**, ***S*-1C** and ***R*-**, ***S*-1MF**. The pattern simulated from the single-crystal data of ***S*-1C** is given for comparison. (b) The IR spectra of ***R*, *S*-1C** and ***R*, *S*-1MF**. (c) Solid-state CD spectra of ***R*-**, ***S*-1C** and ***R*-**, ***S*-1MF**. (d) The inorganic layer of ***S*-1C**. (e) Packing diagram of ***S*-1C** viewed along the *b*-axis. (f) Packing diagram of ***S*-1C** viewed along the *c*-axis.

This journal is © The Royal Society of Chemistry 2025

Published on 10 January 2025. Downloaded on 2/21/2026 7:01:00 PM.

clinic space group $P2_1$. The asymmetric unit contains two In^{3+} ions, two *S*-pempH$^-$, two OH^-, two NO_3^-, and two coordinated water molecules (Fig. S8†). Each In^{3+} ion adopts six-coordination with an octahedral configuration. In1 is coordinated by three phosphonate O atoms (O1, O3A, and O4) from three *S*-pempH$^-$, one O atom (O1W) from one H_2O, and two μ_2-OH^- (O7 and O7A). In2 is coordinated by three phosphonate O atoms (O2, O5, and O6B) from three *S*-pempH$^-$, one O atom (O2W) from one H_2O, and two μ_2-OH^- (O8 and O8C). The In1–O and In2–O bond lengths are 2.081–2.227 Å and 2.090–2.223 Å, respectively (Table S2†). The *S*-pempH$^-$ ligand is protonated at its amino group and acts as a tri-dentate ligand using its three phosphonate oxygen atoms. Each *S*-pempH$^-$ bridges three In atoms and *vice versa*, generating an inorganic layer composed of corner-sharing $\{In(\mu_2\text{-}OH)_2O_4\}$ octahedra and $\{PO_3C\}$ tetrahedra in the *bc* plane (Fig. 1d). Interestingly, the equivalent In1 or In2 atoms are each bridged by μ_2-OH^- units, forming infinite In-OH^- chains of –In1–O7–In1– and –In2–O8–In2–, respectively, which are alternatively arranged along the *c*-direction. Therefore, the inorganic layer of ***S*-1C** can also be viewed as consisting of two kinds of In-OH^- chains interconnected by PO_3 groups. The organic groups of the *S*-pempH$^-$ ligands are suspended on either side of the inorganic layer (Fig. 1e). The hybrid layer is chiral and polar. The equivalent layers are stacked in an AAA manner and unidirectionally along the *a*-axis (Fig. 1e), thus leading to the formation of a polar supramolecular network structure (Fig. 1f). The distance between layers is 18.93 Å. Notably, the NO_3^- counter-anions reside close to the inorganic layer and are H-bonded to the μ_2-OH^- groups (O7 and O8), amino groups (N1 and N2), and coordination water molecules (O1W and O2W) from the same layer (Table S3 and Fig. S9†). The interlayer interactions are dominated by van der Waals contacts.

It is worth mentioning that only ten indium phosphonates have been described in the literature,[26–31] of which three are coordination polymers including two with 2D layered structures[26] and one with a 3D framework structure.[28] Compounds $In(O_3PR)(O_2P(OH)R)\cdot H_2O$ (R = Ph and $PhCH_2$) were supposed to have layered structures based on their PXRD patterns.[26] Notably, chiral indium phosphonates have never been reported. Therefore, compounds ***R*-1C** and ***S*-1C** represent the first examples of chiral indium phosphonates with a new layer topology.

Solvent effect on the morphologies of $In(NO_3)_3$/pempH$_2$ assemblies: formation of *R*-1MF and *S*-1MF microflowers

Previous studies have demonstrated that solvent may have a significant effect on the morphology and even the helicity of chiral coordination polymers.[32–34] Thus, we carried out a systematic study on the assembly of the $In(NO_3)_3$/*S*-pempH$_2$ system using different polar alcohol solvents (MeOH, EtOH, IPA, NPA, and NBA) and alcohol/H_2O mixed solvents. We first conducted the reaction of $In(NO_3)_3\cdot 5H_2O$ and *S*-pempH$_2$ (molar ratio, 1 : 1) in 20, 40, 60, 70, 80, 90, and 100 vol% MeOH/H_2O mixtures (total volume, 10 mL, pH = 3.2, adjusted using triethylene diamine) under solvothermal conditions (100 °C, 1 day) and examined the solid products by scanning electron microscopy (SEM), PXRD, and IR spectroscopy (Fig. S10–S12†). PXRD and IR spectra clearly showed that the product obtained in pure methanol was the unreacted ligand, possibly due to the low solubility of *S*-pempH$_2$ in methanol. Although the products obtained in 20–90 vol% MeOH/H_2O had the same structure as ***S*-1C**, their morphologies were slightly different. The reaction in 20 vol% MeOH/H_2O produced nanoparticles, while that in 40–90 vol% MeOH/H_2O resulted in nanoplates. The nanoplates flocked together but no clear shape was observed.

We next performed the same reaction in 20–100 vol% EtOH/H_2O mixtures (Fig. S13–S15†). Similarly, the product obtained in pure ethanol was dominated by the ligand, while those obtained in 20–90 vol% EtOH/H_2O had the same structure as ***S*-1C**. From their SEM images we can see that the 20–60 vol% products were aggregates of nanoplates/nanosheets with irregular shapes. Interestingly, we observed microparticles composed of aggregated nanosheets in the 80–90 vol% products together with nanoparticles.

When the reaction of $In(NO_3)_3\cdot 5H_2O$ and *S*-pempH$_2$ was conducted in 20–90 vol% NPA/H_2O or IPA/H_2O, we obtained the same product ***S*-1C** (Fig. S16–S21†). Although the products in 20–80 vol% NPA/H_2O were composed of stacked nanosheets with different sizes, the nanosheets in the 90 vol% product aggregated into circular flower-like structures (Fig. S16†). For products obtained in IPA/H_2O, the nanosheets were stacked randomly in the 20–70 vol% products, but formed microparticles with flower-like shapes in the 80–90 vol% products (Fig. S19†). Impressively, in the 90 vol% IPA/H_2O product, we observed uniformly distributed microparticles with an elliptical flower-like structure formed by the stacking of chiral nanosheets.

Finally, we performed the same reaction in 20–100 vol% NBA/H_2O mixed solvents. As shown in Fig. S22,† the 20–60 vol% products showed randomly distributed nanosheets with larger lateral dimensions. In the 70–90 vol% products, the nanosheets aggregated but no clear shape was observed. All products obtained in 20–90 vol% NBA/H_2O are the same as ***S*-1C** (Fig. S23 and S24†).

To sum up, the reaction of $In(NO_3)_3\cdot 5H_2O$ and *S*-pempH$_2$ in 20–90 vol% alcohol/H_2O (alcohol = MeOH, EtOH, NPA, IPA, and NBA) resulted in the same compound as ***S*-1C** with different morphologies. A uniformly distributed product with a flower-like structure can be obtained in 90 vol% IPA/H_2O and was named ***S*-1MF** (MF refers to microflower). If *R*-pempH$_2$ instead of *S*-pempH$_2$ was used in a similar synthesis, we obtained the product ***R*-1MF**. As shown in Fig. 2, the ***S*-1MF** structures exhibit a highly branched and aggregated morphology with distinct left-handed spiral arrangements of the petal layers. In contrast, the ***R*-1MF** structures show a branched and aggregated morphology but feature right-handed spiral configurations of the petal layers.

Both types of microflowers have petals that are layered and relatively thin, with notable chirality in their spiral structures. ***R*-1MF** and ***S*-1MF** are enantiomers, verified by their identical

Published on 10 January 2025. Downloaded on 2/21/2026 7:01:00 PM.

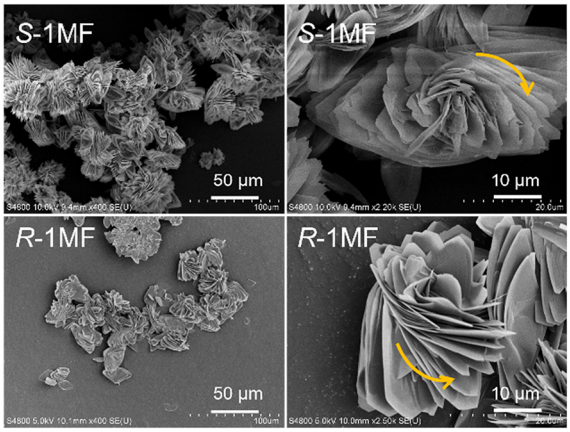

Fig. 2 SEM images of the self-assembled products of $In(NO_3)_3$/*S*-, *R*-pempH$_2$ in 90 vol% IPA/H_2O at 100 °C (***S*-1MF** and ***R*-1MF**).

PXRD patterns and IR and UV-vis spectra (Fig. S4–S6†), as well as CD spectra, which show a dichroic signal at *ca.* 230 nm with an opposite sign (Fig. 1c).

Interestingly, the thickness of the nanosheets obtained in 90 vol% alcohol/H_2O varied with the solvent (Fig. 3). In 90 vol% MeOH/H_2O, the nanosheets have a thickness of approximately 100–200 nm. In a 90 vol% EtOH/H_2O system, the nanosheets exhibit a thickness of around 200–300 nm. The sample synthesized in 90 vol% NPA/H_2O shows more compact and densely packed petals with an estimated thickness of 200–300 nm. The petals observed in the sample in 90 vol% IPA/H_2O are the thinnest, ranging from 50–100 nm. Adjusting the volume fraction of IPA has a significant impact on the size and aggregation of the microflowers. As the IPA ratio increases, the nanosheets become thinner, with reduced aggregation, ultimately leading to a uniformly distributed flower-like structure. In contrast, the nanosheets obtained in 90 vol% NBA/H_2O are the thickest, with an estimated thickness of 300–400 nm. Despite these variations, all samples exhibit identical IR spectra and PXRD patterns (Fig. S25†).

Formation mechanism of *S*-1MF

In order to understand the formation mechanism of microflowers, we further investigated the changes of the $In(NO_3)_3$/*S*-pempH$_2$ assemblies over time in 90 vol% IPA/H_2O at 100 °C. The reaction products of 15 to 60 min were clear solutions without any precipitates. However, TEM images revealed that dispersed sphere-like nanoparticles with sizes ranging from 10 to 30 nm appeared in the 15 min product (Fig. S26†), indicating the onset of the nucleation stage. By 30 min, the nanoparticles grew significantly to 50–100 nm and started to aggregate. At 60 min, they adopted non-spherical shapes with sizes of 300–500 nm. After 60 min of reaction, we observed precipitates, which were used for SEM measurements. As shown in Fig. 4a, the 90 min product contained irregularly shaped nanoparticles with sizes of approximately 500 nm to 1 μm. At 3 h, the particles appeared as irregularly shaped aggregates with noticeable surface textures and protrusions, reaching sizes of 1–5 μm. The nanosheet-like surface texture of the particles (size 1–8 μm) became more significant at 4 h. After 5 h of reaction, the morphology changes significantly, and microscopic structures made of stacked nanosheets can be clearly seen with sizes increasing to 5–10 μm. Loose flower-like aggregates formed after 6 h, with overall sizes of 10–20 μm. By 9 h, the aggregates became larger, forming distinct flower-like structures with overall sizes of 20–25 μm. By 18 h, the flower-like structures became more complex and distinct, with sizes of 25–30 μm and layered petal morphologies. Finally, at 24 h, the self-assembly process results in intricately layered flower-like structures (***S*-1MF**), with overall sizes of 25–35 μm and petal thicknesses of approximately 100 nm, indicating the successful completion of the assembly process at this stage. Throughout the process, as time progresses, there is a clear trend toward increasing size, complexity, and order, with the

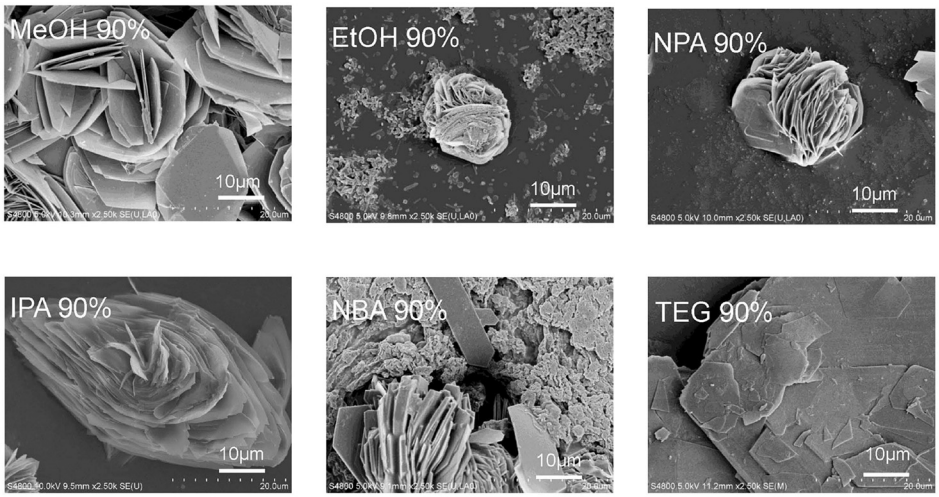

Fig. 3 SEM images of the self-assembled products of $In(NO_3)_3$/*S*-pempH$_2$ in 90 vol% alcohol/H_2O at 100 °C.

This journal is © The Royal Society of Chemistry 2025

Published on 10 January 2025. Downloaded on 2/21/2026 7:01:00 PM.

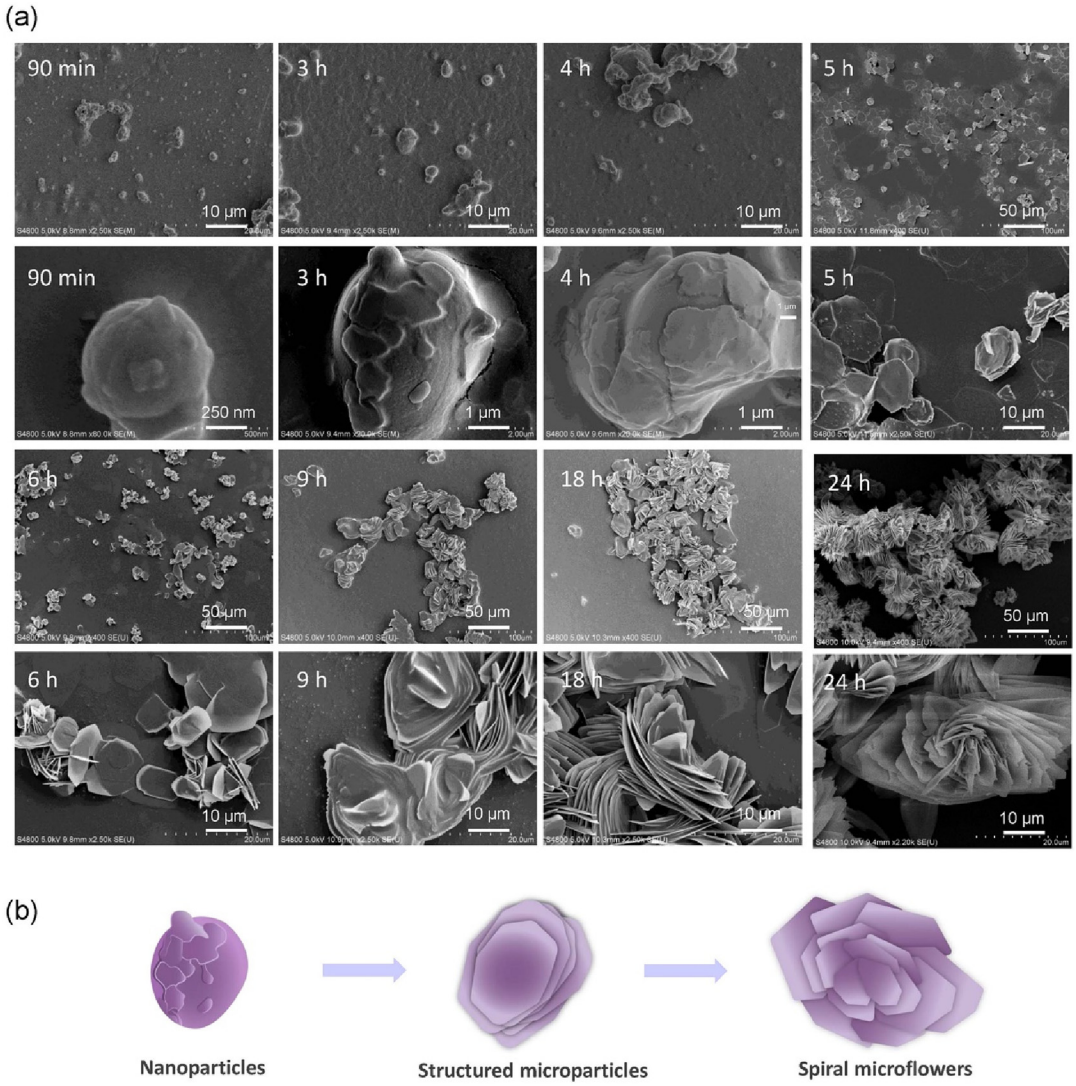

Fig. 4 (a) SEM images of the self-assembled products of $In(NO_3)_3$/*S*-pempH$_2$ in 90 vol% IPA/H_2O at 100 °C for different reaction times. (b) Proposed mechanism for the formation of spiral microflowers.

final structures being highly organized and indicative of the meticulous self-assembly capabilities of the $In(NO_3)_3$/*S*-pempH$_2$ system under the given conditions. We conducted the PXRD and IR measurements for the solid products from reactions lasting between 90 min and 24 h. The results indicate that all products have the same structure as ***S*-1C** (Fig. S27 and S28†).

Based on the above observations, we hypothesize that the formation of microflowers of ***S*-1MF** occurred in three stages (Fig. 4b). First, $In(NO_3)_3$ and *S*-pempH$_2$ reacted in 90 vol% IPA/H_2O to form sphere-like nanoparticles immediately; second, the nanoparticles grew into irregularly shaped micro-particles with the surfaces covered by stacked nanosheets; and third, further reaction and growth of the microparticles led to the formation of spiral microflowers. This process may be driven by surface energy minimization, anisotropic crystal growth, and specific reaction conditions, as suggested by others for the formation of flower-like structures.[35–39] In the present case, the indium phosphonate has a layered structure, in which the interlayer interactions are much weaker than the intralayer interactions. It is therefore to be expected that the $In(NO_3)_3$/*S*-pempH$_2$ assemblies tend to grow anisotropically and form nanosheets, as found for other metal phosphonates.[40] The formation of spiral microflowers of ***S*-1MF** is unusual, which must be attributed to the solvent effect. Compared to other alcohols, the reaction of $In(NO_3)_3$ and *S*-pempH$_2$ in 90 vol% IPA/H_2O produced the thinnest nanosheets or petals. In addition, the interaction between the IPA solvent and the ligand may affect the orientation of the phenyl groups hanging outside the layers.[32] All these factors may contribute to the chiral transcription and amplification during the assembly process of the $In(NO_3)_3$/*S*-pempH$_2$ system and hence the formation of spiral microflowers of ***S*-1MF**.

Published on 10 January 2025. Downloaded on 2/21/2026 7:01:00 PM.

Water stability of *S*-1C and *S*-1MF

Crystalline metal phosphonates and the corresponding nanosheets, especially those with high-valent metal ions, often exhibit high water stability.[41–43] To evaluate the water stability of ***S*-1C** and ***S*-1MF**, we conducted comprehensive stability assessments. As illustrated in Fig. 5, both compounds exhibited remarkable stability when exposed to boiling water for 24 h, indicating their resistance to hydrolysis and structural breakdown under high temperatures. The two samples were also immersed in aqueous solution at different pH values (adjusted using 0.01 M HCl or NaOH) for 24 h. Clearly, they maintained their structures across a wide pH range from 1 to 11 in aqueous solutions, which demonstrates their resilience in both acidic and basic environments (Fig. S29 and S30†). This stability is essential for practical applications, indicating that ***S*-1MF** can withstand harsh conditions, making it a promising candidate for applications in chiral recognition and others.

Chiral recognition properties

Chiral recognition on solid surfaces is important for related applications such as enantiomeric separation and sensing of chiral molecules and heterogeneous asymmetric catalysis.[44,45] The microflowers of ***S*-1MF** and ***R*-1MF** possess much larger surface areas than their crystalline counterparts, as well as domain-limited spaces between the petals. This is confirmed by the N_2 adsorption isotherm measurements at 77 K. As shown in Fig. S31,† at $P/P_0 \approx 0.98$, the adsorption capacities of ***R*-1MF** and ***S*-1MF** for N_2 were 32.72 $cm^3\ g^{-1}$ and 34.51 $cm^3\ g^{-1}$, respectively, which were higher than that of ***S*-1C** (16.01 $cm^3\ g^{-1}$). In addition, the BET surface areas of ***R*-1MF** (12.1 $m^2\ g^{-1}$) and ***S*-1MF** (12.37 $m^2\ g^{-1}$) were also higher than that of ***S*-1C** (7.31 $m^2\ g^{-1}$). Notably, all three samples show rather low BET areas, which is reasonable considering that ***R*-1** and ***S*-1** have a densely packed layered structure. The pore size distribution determined by the BJH method[46] showed three peaks at 1.93, 7.98 and 14.02 nm for ***R*-1MF** and ***S*-1MF**, indicating the presence of both micro- and meso-pores in these materials. In contrast, the pore size of ***S*-1C** is concentrated around 1.29 nm, suggesting the presence of only micropores (Fig. S32†).

To investigate the chiral recognition properties of these materials, adsorption measurements were performed on activated samples of ***S*-1MF**, ***R*-1MF**, and ***S*-1C** using enantiopure *R*-2-butanol and *S*-2-butanol as probe molecules. The adsorption isotherms clearly exhibit enantioselective behaviour. At $P/P_0 \approx 0.98$, the adsorption capacity for *S*-2-butanol on ***S*-1MF** (4.57 $cm^3\ g^{-1}$) is significantly higher compared to ***R*-1MF** (3.06 $cm^3\ g^{-1}$) and ***S*-1C** (3.45 $cm^3\ g^{-1}$) (Fig. 6a). The higher adsorption capacity of ***S*-1MF** in comparison with ***S*-1C** can be explained by the larger surface area of the microflowers than the crystalline sample. Fig. 6b and Fig. S33† demonstrate the differential adsorption of *R*-2-butanol and *S*-2-butanol on ***S*-1MF** and ***R*-1MF**. Apparently, ***S*-1MF** shows much higher adsorption for *S*-2-butanol (4.57 $cm^3\ g^{-1}$) than for *R*-2-butanol (0.86 $cm^3\ g^{-1}$), indicating a clear preference for the *S*-enantiomer. We note that the adsorption of *S*-2-butanol on ***S*-1MF** becomes obvious above $P/P_0 = 0.4$, suggesting a gate-opening effect. Moreover, the adsorption/desorption isotherm shows a large hysteresis, with the desorption of *S*-2-butanol occurring below $P/P_0 = 0.25$. The result suggests that a strong interaction is present between the adsorbent ***S*-1MF** and *S*-2-butanol.

According to the structural description, compound ***S*-1** has a positively charged layer structure, balanced by the NO_3^- anion. The latter forms hydrogen bonds with the coordinated OH^- and water molecules as well as the uncoordinated amino groups of *S*-pempH$^-$ (Fig. 7). As a result, the adjacent 1-phenylethylamino groups of *S*-pempH$^-$ form chiral pockets on the surface of the layer together with the nitrate anion. The chiral guest molecule, *S*-2-butanol, can be inserted into the pocket and interacts with the layer through O–H···O hydrogen-bonding interaction with the nitrate anion and/or C–H···π interaction with the phenyl groups in the layer. Obviously, the small chiral pocket in ***S*-1MF** favours the adsorption of *S*-2-butanol over *R*-2-butanol. This may be the reason why the

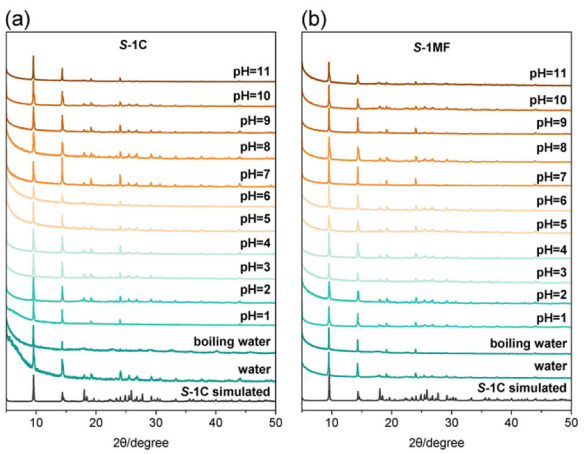

Fig. 5 PXRD patterns of the as-synthesized samples ***S*-1C** (a) and ***S*-1MF** (b) by soaking in water, boiling water and aqueous solutions in the pH range from 1 to 11 for 24 h.

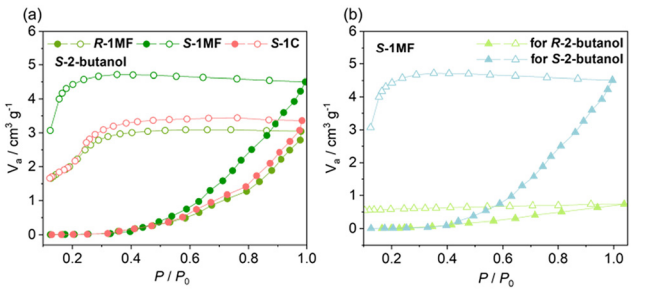

Fig. 6 (a) Comparison of the *S*-2-butanol adsorption (filled)/desorption (open) isotherms for the activated compounds ***R*-1MF**, ***S*-1MF**, and ***S*-1C**. (b) *S*- and *R*-2-butanol adsorption (filled) and desorption (open) isotherms for the activated compound ***S*-1MF** at 298 K.

This journal is © The Royal Society of Chemistry 2025

Published on 10 January 2025. Downloaded on 2/21/2026 7:01:00 PM.

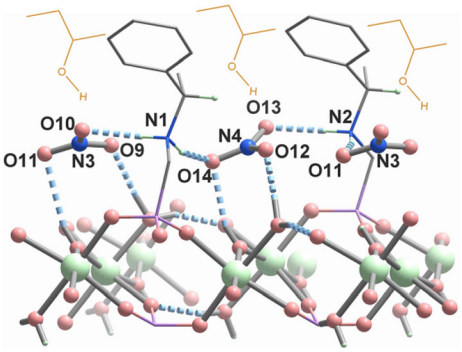

Fig. 7 The proposed adsorption mechanism of *S*-2-butanol (in brown color) on the layer surface of ***S*-1MF**.

adsorption capacity of ***S*-1MF** for *S*-2-butanol is significantly enhanced. PXRD analysis confirmed that the structures of ***S*-1C**, ***S*-1MF**, and ***R*-1MF** were preserved following the adsorption tests (Fig. S34†).

Conclusions

We report the first examples of chiral indium phosphonates, namely *R*-, *S*-$[In_2(pempH)_2(\mu_2\text{-}OH)_2(H_2O)_2](NO_3)_2$ (***R*-**, ***S*-1**), which exhibit layered structures. The morphology of these compounds can be modulated using alcohol/water mixed solvents, leading to crystals of ***R*-**, ***S*-1C** in TEG/H_2O and spiral microflowers of ***R*-**, ***S*-1MF** in IPA/H_2O. The acquisition of ***R*-**, ***S*-1MF** spiral microflowers demonstrates that chirality has been successfully transferred and amplified from the chiral ligand to the layer and finally to the morphology. Interestingly, the spiral microflowers of ***R*-**, ***S*-1MF** are stable in water. Adsorption studies using *R*- and *S*-2-butanol as probing molecules revealed that ***S*-1MF** shows enhanced adsorption capacity in comparison with its crystalline counterpart and pronounced adsorption discrimination properties. This work may encourage further exploration of chiral metal phosphonates with macroscopically chiral morphologies and interesting functions.

Author contributions

Q. T. and R. G. conducted experiments and analysed the data. Q. T. wrote the manuscript. S.-S. B. solved the crystal structure. L.-M. Z. conceived the project and revised the manuscript.

Data availability

The data supporting this article have been included as part of the ESI.†

Conflicts of interest

There are no conflicts to declare.

Acknowledgements

This work was supported by the National Natural Science Foundation of China (92356303 and 21731003).

References

1 X. Niu, R. Zhao, S. Yan, Z. Pang, H. Li, X. Yang and K. Wang, *Small*, 2023, **19**, 2303059.
2 M. Xue, B. Li, S.-L. Qiu and B.-L. Chen, *Mater. Today*, 2016, **19**, 503–515.
3 G. Sun, X. Zhang, Z. Zheng, Z.-Y. Zhang, M. Dong, J.-L. Sessler and C.-J. Li, *J. Am. Chem. Soc.*, 2024, **146**, 26233–26242.
4 X. Shang, I. Song, H. Ohtsu, Y.-H. Lee, T. Zhao, T. Kojima, J.-H. Jung, M. Kawano and J. H. Oh, *Adv. Mater.*, 2017, **29**, 1605828.
5 T. He, I. K. W. On, S. Bi, Z. Huang, J. Guo, Z. Wang and Y. Zhao, *Angew. Chem., Int. Ed.*, 2024, **63**, e202405769.
6 (*a*) S. Das, S. Xu, T. Ben and S.-L. Qiu, *Angew. Chem., Int. Ed.*, 2018, **57**, 8629; (*b*) J.-P. Zhao, J. Luo, Z.-H. Lin, X. Chen, G.-H. Ning, J.-Z. Liu and D. Li, *Inorg. Chem. Front.*, 2022, **9**, 4907–4912.
7 (*a*) X.-H. Niu, Y.-Q. Liu, R. Zhao, M. Yuan, H.-F. Zhao, H.-X. Li and K.-J. Wang, *ACS Appl. Mater. Interfaces*, 2024, **16**, 17361–17370; (*b*) C. Li, X.-X. Yang, M.-Y. Zheng, Z.-G. Gu and J. Zhang, *Adv. Funct. Mater.*, 2024, **34**, 2401102.
8 (*a*) S. Zhang, Y. Zheng, H. An, B. Aguila, C.-X. Yang, Y. Dong, W. Xie, P. Cheng, Z. Zhang, Y. Chen and S. Ma, *Angew. Chem., Int. Ed.*, 2018, **57**, 16754; (*b*) A. Gheorghe, B. Strudwick, D. M. Dawson, S. E. Ashbrook, S. Woutersen, D. Dubbeldam and S. Tanase, *Chem. – Eur. J.*, 2020, **26**, 13957.
9 C.-X. Tan, K.-W. Yang, J.-Q. Dong, Y.-H. Liu, Y. Liu, J.-W. Jiang and Y. Cui, *J. Am. Chem. Soc.*, 2019, **141**, 17685–17695.
10 J. Guo, Y. Zhang, Y. Zhu, C. Long, M. Zhao, M. He, X. Zhang, J. Lv, B. Han and Z.-Y. Tang, *Angew. Chem., Int. Ed.*, 2018, **57**, 6873.
11 B. Shen, Y. Kim and M. Lee, *Adv. Mater.*, 2020, **32**, 1905669.
12 Y.-H. Liu, L.-M. Liu, X. Chen, Y. Liu, Y. Han and Y. Cui, *J. Am. Chem. Soc.*, 2021, **143**, 3509–3518.
13 H.-J. Jiang, L. Zhang, J. Chen and M.-H. Liu, *ACS Nano*, 2017, **11**, 12453–12460.
14 Y. Jin, C. Xiao, L. Tan, Z. Chen, Z. Wen, Y. Cheng, W. Fu and P. Wang, *Adv. Opt. Mater.*, 2023, **11**, 2203068.
15 (*a*) K. Ding, J. Ai, Q. Deng, B. Huang, C. Zhou, T. Duan, Y. Duan, L. Han, J. Jiang and S. Che, *Angew. Chem., Int. Ed.*, 2021, **60**, 19024; (*b*) Y.-Y. Duan, X. Liu, L. Han, S. Asahina,

Published on 10 January 2025. Downloaded on 2/21/2026 7:01:00 PM.

D.-D. Xu, Y.-Y. Cao, Y. Yao and S. Che, *J. Am. Chem. Soc.*, 2014, **136**, 7193–7196.
16 B. Zhao, H.-L. Yu, K. Pan, Z. Tan and J.-P. Deng, *ACS Nano*, 2020, **14**, 3208–3218.
17 *Metal Phosphonate Chemistry: From Synthesis to Applications*, ed. A. Clearfield and K. Demadis, The Royal Society of Chemistry, 2012.
18 S. J. Shearan, N. Stock, F. Emmerling, J. Demel, P. A. Wright, K. D. Demadis, M. Vassaki, F. Costantino, R. Vivani, S. Sallard, I. R. Salcedo, A. Cabeza and M. Taddei, *Crystals*, 2019, **9**, 270.
19 (*a*) S.-S. Bao, M.-F. Qin and L.-M. Zheng, *Chem. Commun.*, 2020, **56**, 12090–12108; (*b*) T. Zheng, W. Tan and L.-M. Zheng, *Acc. Chem. Res.*, 2024, **57**, 2973–2984.
20 G.-G. Weng and L.-M. Zheng, *Sci. China: Chem.*, 2020, **63**, 619–636.
21 X.-G. Liu, S.-S. Bao, Y.-Z. Li and L.-M. Zheng, *Inorg. Chem.*, 2008, **47**, 5525–5527.
22 Z.-M. Zhai, T. Hou, Y. Xu, Q. Teng, S.-S. Bao and L.-M. Zheng, *Chem. – Eur. J.*, 2025, **31**, e202403699.
23 *SAINT, version 8.40A, Program for Data Extraction and Reduction*, Bruker Nano., Inc., 2019.
24 G. M. Sheldrick, *SHELXT*, 2014/5, 2014; *SHELXL* 2018/3, 2018.
25 Y. Inokuchi and N. Nishi, *J. Chem. Phys.*, 2001, **114**, 7059–7065.
26 J. Morizzi, M. Hobday and C. Rix, *J. Mater. Chem.*, 1999, **9**, 863–864.
27 A. F. Richards and C. M. Beavers, *Dalton Trans.*, 2012, **41**, 11305–11310.
28 W.-Y. Dan, X.-F. Liu, M.-L. Deng, Y. Lin, Z.-X. Chen and Y.-M. Zhou, *Dalton Trans.*, 2015, **44**, 3794–3800.
29 V. Chandrasekhar, J. Goura and A. Duthie, *Inorg. Chem.*, 2013, **52**, 4819–4824.
30 Y. Y. Enakieva, M. V. Volostnykh, S. E. Nefedov, G. A. Kirakosyan, Y. G. Gorbunova, A. Y. Tsivadze, A. G. Bessmertnykh-Lemeune, C. Stern and R. Guilard, *Inorg. Chem.*, 2017, **56**, 3055–3070.
31 A. Kechiche, S. A. Shehimy, L. Khrouz, C. Monnereau, C. Bucher, S. Parola, A. Bessmertnykh-Lemeune, Y. Rousselin, A. V. Cheprakov and H. Nasri, *Dalton Trans.*, 2024, **53**, 7498–7516.
32 J.-G. Jia, C.-C. Zhao, Y.-F. Wei, Z.-M. Zhai, S.-S. Bao, A. J. Jacobson, J. Ma and L.-M. Zheng, *J. Am. Chem. Soc.*, 2023, **145**, 23948–23962.
33 G.-G. Weng, X.-D. Huang, R. Hu, S.-S. Bao, Q. Zou, G.-H. Wen, Y.-Q. Zhang and L.-M. Zheng, *Chem. – Asian J.*, 2021, **16**, 2648–2658.
34 T. Hou, C.-C. Zhao, S.-S. Bao, Z.-M. Zhai and L.-M. Zheng, *Dalton Trans.*, 2024, **53**, 4291–4298.
35 S.-Q. Zhang, L.-N. Li, S.-G. Zhao, Z.-H. Sun, M.-C. Hong and J.-H. Luo, *J. Mater. Chem. A*, 2015, **3**, 15764–15768.
36 M. Rashid, S. Parsaei, A. Ghoorchian, K. Dashtian and D. Mowla, *J. Ind. Eng. Chem.*, 2023, **121**, 275–286.
37 S.-L. Zhong, Z.-G. Zou, S.-J. Lv, S.-C. Zhang, J. Geng, J.-Y. Meng, X. Liu, F.-G. Liang and J.-J. Rao, *J. Alloys Compd.*, 2022, **903**, 163845.
38 N. Roy, H. R. Barai, A. N. Banerjee, J. S. Kim and S. W. Joo, *Chem. Eng. Sci.*, 2023, **277**, 118834.
39 J. Wang, J. Yang, H. Yang, H.-Z. Huang, X.-D. Yang and L. Wei, *Opt. Mater.*, 2023, **135**, 113303.
40 Z.-S. Cai, Y. Shi, S.-S. Bao, Y. Shen, X.-H. Xia and L.-M. Zheng, *ACS Catal.*, 2018, **8**, 3895–3902.
41 Y. Huang, F. Zhou, J. Feng, H. Zhao, C. Qi, J. Ji, S. Bao and T. Zheng, *Chem. Commun.*, 2021, **57**, 1238–1241.
42 G.-H. Wen, X.-M. Chen, K. Xu, X. Xie, S.-S. Bao and L.-M. Zheng, *Dalton Trans.*, 2021, **50**, 17129–17139.
43 (*a*) M.-F. Qin, Q.-Q. Mu, S.-S. Bao, X. Liang, Y. Peng and L.-M. Zheng, *ACS Appl. Energy Mater.*, 2021, **4**, 4319–4326; (*b*) M.-F. Qin, L.-F. Zheng, S.-S. Bao, F.-H. Xue, J. Su, J. Ma and L.-M. Zheng, *ACS Appl. Electron. Mater.*, 2023, **5**, 887–895.
44 J. Sui, N. Wang, J. Wang, X. Huang, T. Wang, L. Zhou and H. Hao, *Chem. Sci.*, 2023, **14**, 11955–12003.
45 G. Li, Q. Yang, K. Manna, Y. Zhang, P. Merz, C. Shekhar, Y. Zhang, H. Lv, A. Markou, Y. Sun and C. Felser, *Angew. Chem., Int. Ed.*, 2023, **62**, e202303296.
46 M. Thommes, K. Kaneko, A. V. Neimark, J. P. Olivier, F. Rodriguez-Reinoso, J. Rouquerol and K. S. Sing, *Pure Appl. Chem.*, 2015, **87**, 1051–1069.

This journal is © The Royal Society of Chemistry 2025